Theoretical and Computational Acoustics
D. Lee, Y-H Pao, M.H. Schultz, and Y-C Teng (Editors)

Noise Cancellation by Arrays of Active Noise Sources in Enclosures with Impedance Surfaces

G. Rosenhouse and E. Saski
Faculty of Civil Engineering, Technion-Israel Institute of Technology
Haifa, 32000, Israel

Abstract

The paper presents a new computer program for calculation and graphical display of sound fields caused by sound sources in enclosed spaces. For the simulation purposes the sources include monopoles, dipoles, quadrupoles etc as primary and secondary sources. We describe the sound field affected by rigid and absorbing boundaries, introducing the mathematical complexity due to the complex spherical wave reflection over highly absorbing areas. Next, impedance boundary effects are analyzed by an exact integral solution where necessary and in other cases by an approximate formulation based on "image" sources using complex reflection coefficients. The simulation program is then used to describe sound fields within enclosures containing a desired number of absorbing walls. Engineering and physical conclusions summarize the present work, including descriptions of the sound fields of interest.

1. Introduction

Active noise control within enclosures is involved not only with the superposition of sound fields caused by various sources, but also with reflections which add a diffusive field to the direct one. This combination increases considerably the complexity of the sound fields of both primary and secondary sources that serve the Active Noise Control (ANC). ANC is involved with multi-reflections effects not only because of the boundaries in the domain, but also due to all other obstacles in the examined environment that can be influential. Such sound reflections strongly distort the sound field in a way that might be understood only by a global view of the domain, as will be demonstrated in this paper.

There are many analysis methods for simulation of sound fields within enclosures. Basic reference books on room acoustics in this context are those of Cremer, Mueller and Schultz (1978) and Kuttruff (1976).

These methods include:

Ray tracing methods: The physical fundamentals of the methods and historical background are given in Pierce (1981). Specific publications on the use of these methods in acoustical analyses of auditoria were presented for example by Schroeder (1970), Santon (1976), Krokstad et al. (1968, 1983) and Sekiguchi, et al. (1985).

Image sources methods: Juricic and Santon (1973) and Gensane and Santon (1979). A more advanced theory, but with the deficiency of too many image sources at high order reflections was presented by Sakurai (1987), who superposed the response from reflected sounds from rigid plane panels, using the line integral formulation based on

Kirchhoff's formula and Kirchhoff's boundary conditions. Rosenhouse and Saski (1995) modified the image source method to enclosures with several sound absorbing impedance surfaces of high absorption coefficients.
Numerical techniques: Problems with complicated domains, such as obstacles within the enclosure, are more reasonably solved by numerical techniques like the Finite Element Method (FEM) combined with modal analysis, Migeot (1993) and the Boundary Element Method (BEM) for steady state and transient fields respectively - Terai, T., Kawai in the book of Ciskowski and Brebbia (1991).
Modal analysis combined with minimization: See Nelson and Elliott (1992).
In the present paper we apply the image sources method in empty rooms, where the direct sound and the effect of reflections from the wall surfaces within the enclosures are taken into account and some surfaces are highly sound absorbing. Various case studies show the possibility of using the method as an aid for design based on general understanding of source locations effect and the enclosure shape and properties. It brings us to concepts of modern control. Toady's control methodologies enable the computer "see" by guess technologies more than people can see. The computer can find today the clear picture of hidden phenomena by techniques of eliminating noise and observing meaningful clues and dots. The human brain can also draw conclusions by observing trends and clues, and even to some extent "intuition". The rest of the paper develops the technology and illustrates some sound fields created by a combination of primary and secondary sources, in various configurations, to show possibilities of active noise control in enclosures, saving a lot of computational minimization effort.

2. The choice between modal analysis based on rays reflected from impedance surfaces

A main difference between sound radiation in an enclosure and sound radiation in a free space is the existence of multi-reflections in enclosures due to the bounding surfaces, that should be considered carefully. Hence, an essential element in the analysis of a sound field in an enclosure is the reflection of sound from a sound absorbing surface. The strength and the directivity of the reflections and the natural modes of the enclosure depend on the boundary conditions that are attributed to the bounding surfaces. Both modal analysis and ray theories of room acoustics are possible and useful for different analysis purposes.
Generally, modal analysis is not common in room acoustics because of the overwhelming number of eigen frequencies and normal modes involved (about 10^9 within the audio frequency domain). This situation does not enable an adequate acoustic estimation for design purposes. To this fact one should add the difficulties due to possible complexities in the room's geometry, including coupling between rooms and surface irregularities.
The approach based on sound rays and their reflection may be considered relatively simple, and we use it to illustrate sound fields in enclosures for Active Noise Control (ANC) design. The effect of multi-reflections of sound waves from impedance surfaces and their influence on ANC was discussed in detail by Rosenhouse and Saski (1995 - Active 95) and Chapter 3. It appears that when the sound absorption coefficient of a surface is small, it is possible to use an image source, taking into account complex surface impedance and complex absorption coefficient (Ingrad and Morse, 1968), which is simple to use. On the other hand, the reflection from highly absorbing surfaces

is much more complicated and necessitates an exact solution (Thomasson, 1977). The two types of solutions will be used simultaneously in the next section in order to find a solution which is within a prescribed margin of error and also reasonably easy and convenient for use.

3. Sound fields in enclosures with impedance surfaces

A typical room consists mostly of one or two highly absorbing surfaces (walls, ceilings, floors) while the other surfaces absorb very little acoustic energy - See figure 1 for the scheme. After establishing the sound reflection model of the various kinds of surfaces of the room, the comprehensive model of the sound field analysis in enclosure can be built. That includes all the reflecting surfaces, using geometrical acoustics and application of image sources. The following assumptions on which this model is based include:

* Using the principles of geometrical acoustics, reflections of sound from rigid surfaces are considered mirror reflections. It means that instead of considering the whole reflector, image sources represent its effect on the internal sound field.
* Reflections from low absorption surfaces are included in the cases where mirror images are considered. However, under such circumstances the reflection coefficient becomes complex.
* Calculation of reflections from a highly absorbing surface can be correctly derived only by using an exact solution. The pattern of reflection from such surfaces is usually very scattered, which justifies the application of the exact solution under those conditions in spite of the significant increase in the complexity of the mathematical expressions involved.
* After a sound ray hits a highly absorbing surface, in our model the higher order reflections from the neighboring reflecting surfaces are ignored, since only an insignificant error occurs This assumption is also a condition for terminating the series of reflections. Last limitation is schematically illustrated in figure 2.

As a result of the last assumption, the sound field of a room will be derived considering first and second order image sources, in accordance with its geometry. The first model of analysis of the velocity potential ψ in the room assumes that the room surfaces are of a low absorption coefficient, which allows for application of an "approximate method" which will be described latter in this paper. Next we assume that one of the surfaces (number 1), is highly absorbent, which necessitates application of the "exact model". In our examples, the source which is located at (x_0, y_0, z_0), radiates a pure tone of 300 Hz. We assume that the velocity of sound propagation in air is 340 m/s. The room has a box shape of the dimensions X, Y, Z and a receiver is located in it at (x, y, z).

The calculation initiates with estimation of the direct radiation of sound:

$$\psi = \frac{\exp(ikR)}{4\pi R}; \quad R = \sqrt{(x-x_0)^2 + (y-y_0)^2 + (z-z_0)^2}$$

Next, reflections of the first order from the 6 reflecting surfaces n=1 are calculated:

$$\psi'_n = C_m \frac{\exp(ikR'_n)}{4\pi R'_n}; \quad n = 1,2,\ldots,6$$

$$C_m = \frac{\varsigma_n \cos(\theta_n) - 1}{\varsigma_n \cos(\theta_n) + 1}; \quad \cos(\theta_n) = \frac{h_n}{R'_n};$$

$$h_1 = z + z_0;\ h_2 = y + y_0;\ h_3 = x + x_0;\ h_4 = 2Z - z_0 - z;\ h_5 = 2Y - y_0 - y;\ h_6 = 2X - x_0 - x$$

$$R'_1 = \sqrt{(x - x_0)^2 + (y - y_0)^2 + h_1^2}; \quad R'^1_2 = \sqrt{(x - x_0)^2 + h_2^2 + (z - z_0)^2};$$

$$R'_3 = \sqrt{h_3^2 + (y - y_0)^2 + (z - z_0)^2}; \quad R'_4 = \sqrt{(x - x_0)^2 + (y - y_0)^2 + h_4^2};$$

$$R'_5 = \sqrt{(x - x_0)^2 + h_5^2 + (z - z_0)^2}; \quad R'_6 = \sqrt{h_1^2 + (y - y_0)^2 + (z - z_0)^2}$$

Now the second order reflections are calculated as already given in Rosenhouse and Saski (1995 - Active 95) and chapter 3 for reflections from two adjacent reflecting surfaces. However, when the surfaces are parallel we have two possible reflections instead of one. See figure 3. The resulting formulae are:

$$\psi''_{mn} = C'_{mn} C'_m \frac{\exp(ikR''_{mn})}{4\pi R''_{mn}}; \quad n = 1,2,\ldots,6$$

$$C'_{mn} = \frac{\varsigma_m \cos(\theta'_m) - 1}{\varsigma_m \cos(\theta'_m) + 1}; \quad C'_m = \frac{\varsigma_n \cos(\theta'_n) - 1}{\varsigma_n \cos(\theta'_n) + 1}$$

For parallel surfaces we have the following source receiver distances:

$h_{14} = 2Z - z + z_0;\ h_{25} = 2Y - y + y_0;\ h_{36} = 2X - x + x_0;$

$h_{41} = 2Z - z_0 + z;\ h_{52} = 2Y - y_0 + y;\ h_6 = 2X - x_0 + x$

The corresponding distances are:

$$R''_{12} = \sqrt{(x - x_0)^2 + h_2^2 + h_1^2}; \qquad R''_{13} = \sqrt{h_3^2 + (y - y_0)^2 + h_1^2};$$

$$R''_{14} = \sqrt{(x - x_0)^2 + (y - y_0)^2 + h_{14}^2}; \quad R''_{15} = \sqrt{h_6^2 + (y - y_0)^2 + h_1^2};$$

$$R''_{23} = \sqrt{h_3^2 + h_2^2 + (z - z_0)^2}; \qquad R''_{24} = \sqrt{(x - x_0)^2 + h_2^2 + h_4^2}$$

$$R''_{25} = \sqrt{(x - x_0)^2 + h_{25}^2 + (z - z_0)^2}; \quad R''_{26} = \sqrt{h_6^2 + h_2^2 + (z - z_0)^2};$$

$$R''_{34} = \sqrt{h_3^2 + (y - y_0)^2 + h_4^2}; \qquad R''_{35} = \sqrt{h_3^2 + h_5^2 + (z - z_0)^2};$$

$$R''_{36} = \sqrt{h_{36}^2 + (y - y_0)^2 + (z - z_0)^2}; \quad R''_{41} = \sqrt{(x - x_0)^2 + h_5^2 + h_4^2}$$

$$R''_{45} = \sqrt{(x - x_0)^2 + h_5^2 + h_4^2}; \qquad R''_{46} = \sqrt{h_6^2 + (y - y_0)^2 + h_4^2};$$

$$R''_{52} = \sqrt{(x - x_0)^2 + h_{52}^2 + (z - z_0)^2}; \quad R''_{56} = \sqrt{h_6^2 + h_5^2 + (z - z_0)^2};$$

$$R''_{63} = \sqrt{h_{63}^2 + (y - y_0)^2 + (z - z_0)^2};$$

The angles to be calculated depend on the order of reflection of the rays. This implies that we have to compare for each case the geometrical measures, D_{mn} and D^0_{mn}. Using those quantities we have for $D_{mn} > D^0_{mn}$:

$$\cos(\theta_{m'}) = \frac{h_m}{R''_{mn}} \quad \text{and} \quad \cos(\theta_n) = \frac{h_n}{R''_{mn}}$$

Otherwise:

$$\cos(\theta_{m'}) = \frac{h_n}{R''_{mn}} \quad \text{and} \quad \cos(\theta_n) = \frac{h_m}{R''_{mn}}$$

The definitions of D_{mn} and D^0_{mn} are respectively:

$$D_{12} = \frac{h_2}{h_1} z_0; D_{13} = \frac{h_3}{h_1} z_0; D_{15} = \frac{h_5}{h_1} z_0; D_{16} = \frac{h_6}{h_1} z_0$$

$$D_{23} = \frac{h_3}{h_2} z_0; D_{24} = \frac{h_4}{h_2} z_0; D_{26} = \frac{h_6}{h_2} z_0; D_{34} = \frac{h_4}{h_3} z_0$$

$$D_{35} = \frac{h_5}{h_3} z_0; D_{45} = \frac{h_5}{h_4}(Z - z_0); D_{46} = \frac{h_6}{h_4}(Z - z_0); D_{46} = \frac{h_6}{h_4}(Z - z_0); \quad \text{and}$$

$$D^0_{12} = y_0; D^0_{13} = x_0; D^0_{15} = Y - y_0; D^0_{16} = X - x_0; D^0_{23} = x_0; D^0_{24} = Z - z_0;$$

$$D^0_{26} = X - x_0; D^0_{34} = Z - z_0; D^0_{35} = Y - y_0; D^0_{45} = Y - y_0; D^0_{46} = X - x_0; D^0_{56} = X - x_0;$$

For parallel surfaces we have:

$$\cos(\theta'_m) = \cos(\theta'_n) = \frac{h_{mn}}{R''_{mn}}$$

The solution for a highly absorbent boundary (surface number 1 in figure 1 follows the exact representation - see Rosenhouse and Saski (1995 - Active 95). From figures 4, 5 we chose for illustration the situation given in figure 4. This situation yields the following expressions for calculating the resulting sound field. The total sound radiation is involved with four components of the velocity potential:

$$\psi = \psi_0 + \psi'_1 + \psi'_2 + \psi'_3$$

The first term stands for the direct radiation of sound:

$$\psi_0 = \frac{\exp(ikR)}{4\pi R}$$

The second expression is due to the first order reflection from surface 1:

$$\psi'_1 = \frac{\exp(ikR'_1)}{4\pi R'_1} + \psi_{SD} + \psi_B$$

The third expression is the first order reflection from the second surface:

$$\psi'_2 = \frac{\exp(ikR'_2)}{4\pi R'_2}$$

The last expression represents the reflection of the second order, namely:

$$\psi''_{12} = \left\{ \frac{\exp(ikR''_{12})}{4\pi R''_{12}} + \psi'_{SD} + \psi'_B \right\} C'_{r2}$$

To summarize, the reflection of sound from surface 1 is calculated following the "exact solution". In its expression, ψ_{SD} and ψ_B are terms from the solution shown by Thomasson, taking into account the effects of the real source S and its image S'_1. The reflection from surface 2 is based on the reflection coefficient C_{r2} for the incidence angle θ_2. In addition, ψ'_{SD} and ψ'_B, are the corresponding terms of the solution

presented by Thomasson, taking into account the image sources S_2' and S_{12}''. S_2' is the real source suitable for surface 1, after being reduced by the reflection coefficient C_{r2}' for the incidence angle θ_2'.

4. Examples

The aforementioned theory is used now for calculation of some examples of reflections up to the second order, as discussed below. The active control simulation is represented here by the set of secondary sources and the superposition of their fields with that of the primary source. Surface 1 in figure 1 has the following specific impedance components:

$$\Re(\varsigma) = \Im(\varsigma) = 14$$

while those surfaces of low sound absorption acquire the values:

$$\Re(\varsigma) = \Im(\varsigma) = 1000$$

Figure 6 shows the sound field of a monopole within the enclosure. A radial sound radiation pattern is observed.It is seen that the decay of sound from the source outwards is not smooth any more, but some interference obstructions appear close to the location of the source, and practically disappear at a certain distance.

Now we introduce an additional secondary monopole source in anti-phase with the primary source, as depicted in figures 7, 8, 9. In figure 7 we observe that the sound level is reduced in a strip-like domain which is normal to the axis between the sources. If the additional auxiliary source is moved closer to the primary source, as in figure 8, stronger attenuation is achieved at points which are far from both sources, and the domain of higher noise level in the vicinity of the sources becomes smaller. If the additional monopole is located apart from the primary source, as in figure 9, the sound field mapping changes significantly, but no general contribution to the noise reduction is obtained by the secondary control unit.

An introduction of secondary dipole and quadrupole sources as shown in figures 10, 11 yields a slight reduction of the levels of the primary source field at regions far from the source.

Next, we consider an addition of two secondary monopole sources in the vicinity of the primary source as in figure 12, each of half the strength of the primary source and in anti-phase to it. Once again we see that the sound field is reduced significantly.

Finally, a test of five anti-phased monopoles each with fifth the strength of the primary source were placed in the vicinity of the primary source, as in figure 13. We see that in this case the sound field is greatly attenuated. This last result is in agreement with the theoretical approach of canceling the sound field created by a primary noise source. This theory suggests that a large number of anti-phased sources of exactly the same strength as of the primary source can cancel the

5. Summary

This paper studies active noise cancellation in a typical room. Such a room consists of one or two absorbing boundaries, while the rest of the boundaries are practically not absorbing. The model is based on the following assumptions:

* Reflection from a rigid boundary is taken as an "optical" mirror reflection. Here, the common "image source" is used.

* A reflection from a boundary with a low absorption coefficient is involved with a complex reflection coefficient. Yet, a usual "image source" can replace the reflecting surface.
* A reflection from a boundary of high sound absorption coefficient necessitates an application of the "exact" solution, which is characterized by a dispersed reflection.

Some of the results are:

- When an acoustic monopole acts in a room, the radial pattern fits an omni-directional source, but it is not characterized by the ever decreasing circular domains, emanating from the source. First, the levels decrease, and then overcome a number of disturbances, to become virtually constant at a certain distance from the source.
- adding secondary sources in an anti-phase leads to the following results:
  a. The sound levels are reduced in a strip normal to the axis between the sources.
  b. If the auxiliary sources are moved to the vicinity of the primary source a significant attenuation is observed in the far sound field, and the domain of high level in the near field is significantly reduced in size.
- an introduction of a secondary dipole source and a secondary quadrupole source in the vicinity of the primary source, leads to only a slight reduction in the levels in regions which are far from the source.
- A significant reduction in the sound field is obtained by adding two secondary monopole sources which are close to the location of the primary source and are half its strength.
- five monopole sources surrounding the primary source, each with a fifth of the strength of the primary source, cause a large attenuation of the sound field. This result is close to the theoretical approach of annihilating the sound field caused by a source of noise by surrounding it with a large number of auxiliary anti-phased sources.

6. References

1. . Antes, H., Applications in environmental noise, Chapter 11 in: Ciskowski, R.D., Brebbia, C.A. (editors), Boundary Element Methods in Acoustics, Computational Mechanics Publications- Southampton and Boston and Elsevier Applied Science - London and New-York, 1991
2. Ciskowski, R.D., Brebbia, C.A. (editors), Boundary Element Methods in Acoustics, Computational Mechanics Publications- Southampton and Boston and Elsevier Applied Science - London and New-York, 1991
3. Cremer, L., Mueller, H.A., Schultz, T.J., Principles and Applications of Room Acoustics, Applied Science Publishers, London & NY, 1982, volumes 1 and 2
4. Gensane, M., Santon, F., Predicting of sound fields in rooms of arbitrary shape: validity of the image sources method, Jr. Sound Vib., 63, 1979, 97-108
5. Juricic, H., Santon, F., Images et rayons sonores dans le calcul numerique des echogrammes, Acustica, 28, 1973, 77-89
6. Krokstad, A., Strom, S., Sorsdal, S., Calculating the acoustical room response by the use of ray tracing technique, Jr. Sound Vib., 8, 1968, 118-125
7. Krokstad, A., Strom, S., Sorsdal, S., Fifteen years' experience with computerized ray tracing, Appl. Acoust., 16, 1983, 291-312
8. Kuttruff, H., Room Acoustics, Applied Science Publishers, London, 1976
9. Migeot, J.-L., Active noise control of a car interior, SYSNOISE application note 26, 19.10.1993
10. Morse, P.M., Ingrad, K.U., Theoretical Acoustics, McGraw-Hill, NY, 1968, 259 -263

11.Nelson, P.A., Elliott, S.J., Active Control of Sound, Academic Press, London, 1992
12.Pierce, A.D., Acoustics, McGraw-Hill, NY, 1981. Ch. 8: Ray acoustics
13.Rosenhouse, G., Saski, E., Noise cancellation by use of arrays of active noise sources in the vicinity of impedance surfaces, Active 95, Newport beach, CA, USA, 6.81995, 685-696
14.Santon, F., Numerical prediction of echograms and of the intelligibility of speech in rooms, Jr. Acoust. Soc. Am., 59, 1976, 1399-1405
15.Sakurai, Y., The early reflections of the impulse response in an auditorium, J. Acoust. Soc. Jpn. (E), 8, 1987, 127-138
16.Schroeder, M.R., Digital simulation of sound transmission in reverberant spaces, Jr. Acoust. Am., 47, 1970, 424-431
17.Sekiguchi, K., Kimura, S., Sugiyama, T., Approximation of impulse response through computer simulation based on finite sound ray integration, J. Acoust. Soc. Am. Jpn. (E), 6, 1985, 103-115
18.Terai, T., Kawai, Y., BEM applications in room acoustics, Chapter 10 in: Ciskowski, R.D., Brebbia, C.A. (editors), Boundary Element Methods in Acoustics, Computational Mechanics Publications- Southampton and Boston and Elsevier Applied Science - London and New-York, 1991
20..Thomasson, S.I., Reflection of waves from a point source by an impedance boundary, Jr. Acoust. Soc. Am., 59, 4, 1976, 780-785

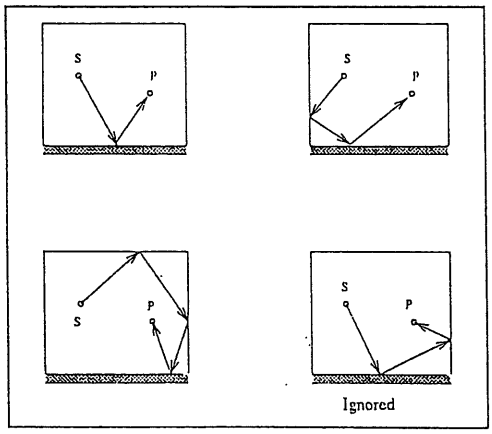

Figure 2. A model of a highly absorbing surface in a room and the relevant reflections

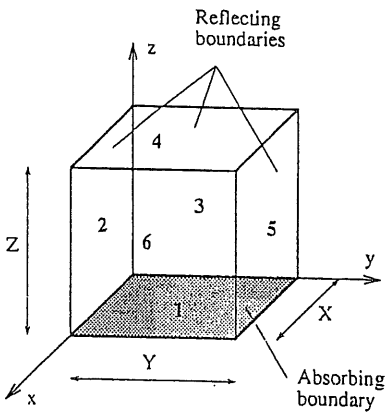

Figure 1. Configuration of a typical room

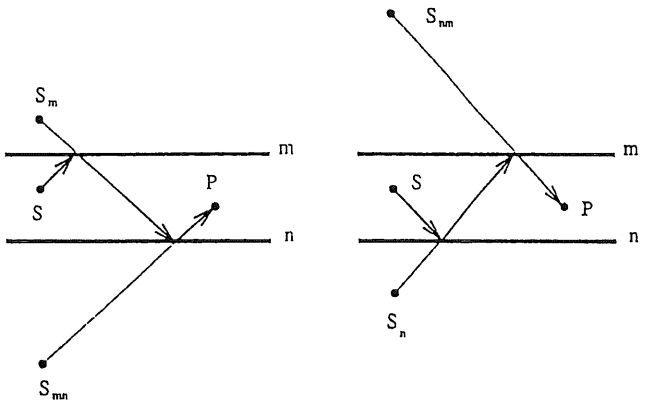

Figure 3. Two types of possible reflections between parallel walls

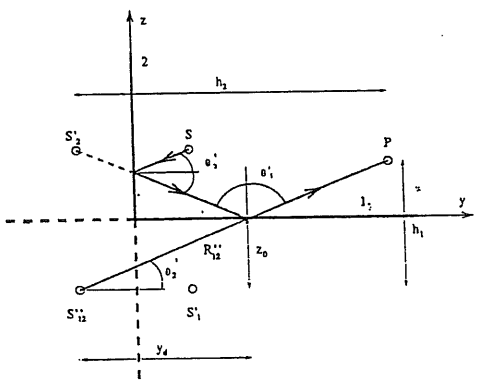

Figure 4. Second order effects: Case A

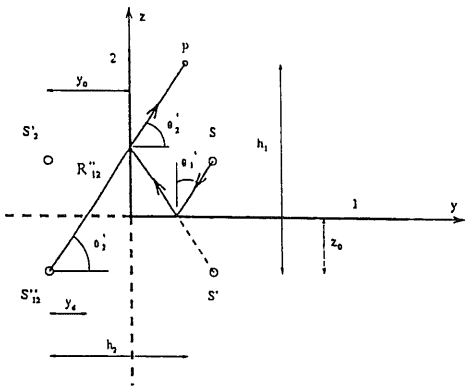

Figure 5 Second order effects: Case B

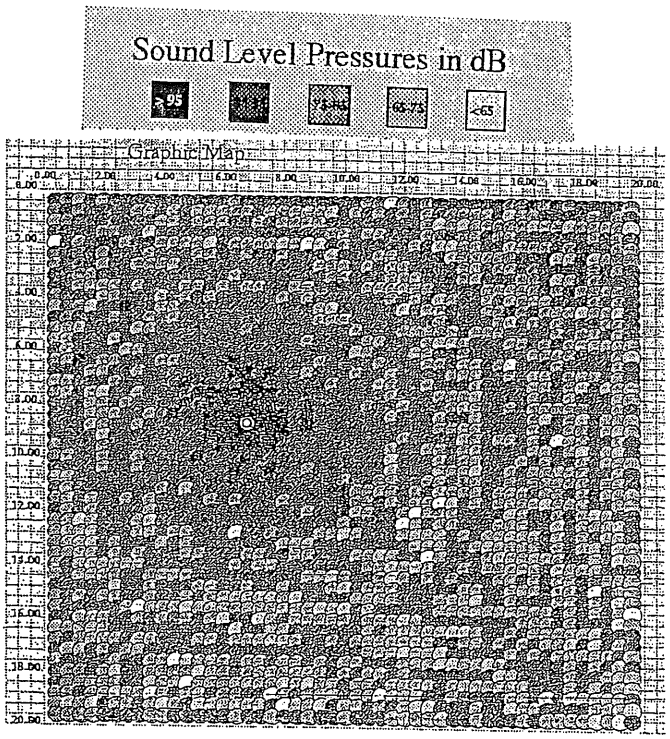

Figure 6. Primary sound field in an enclosure

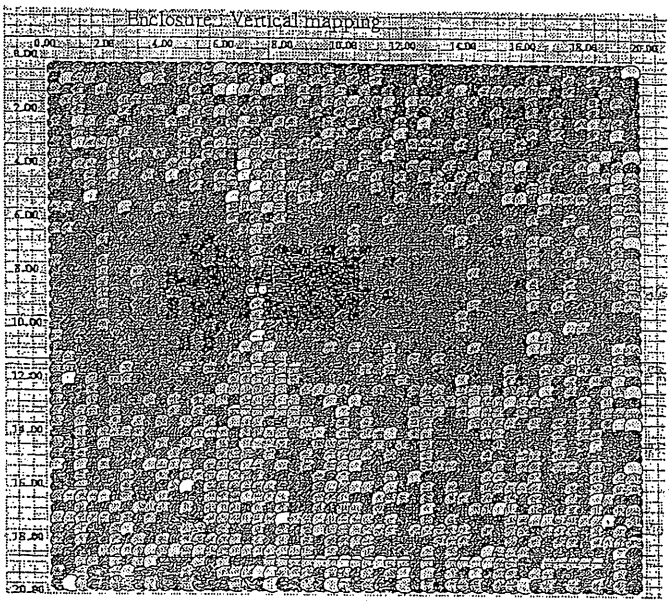

Figure 7. Sound field when a secondary monopole is close to the primary source

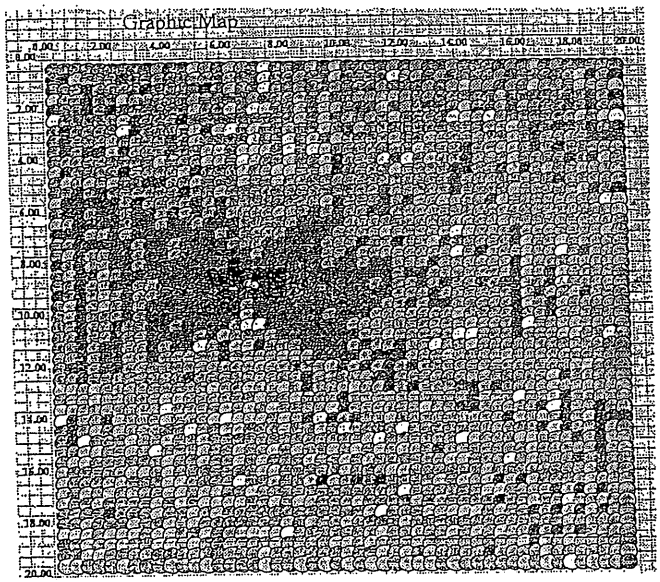

Figure 8. Sound field when a secondary monopole is very close to the primary source

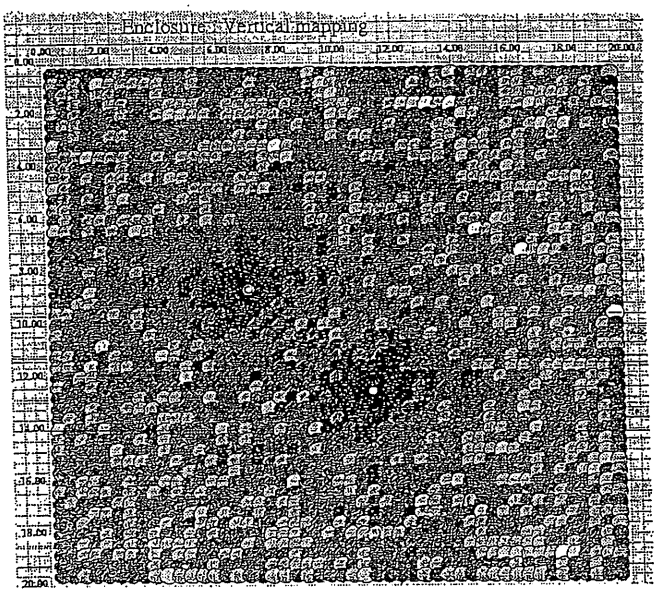

Figure 9. Sound field when a secondary monopole is far from the primary source

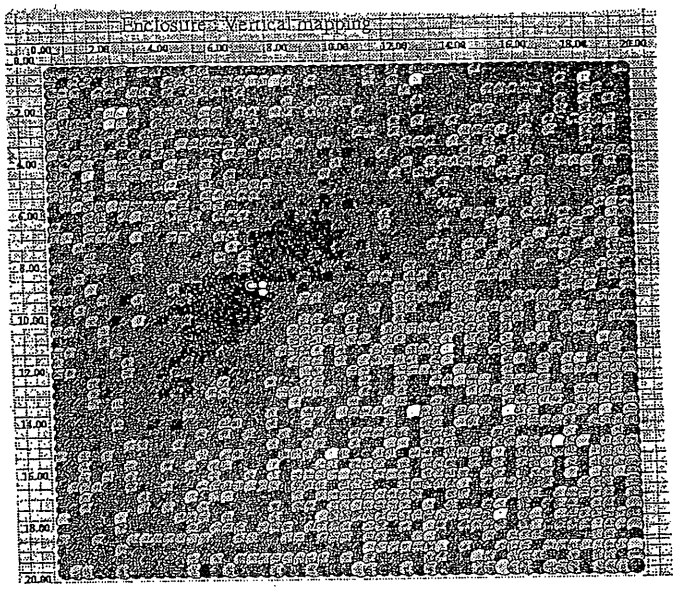

Figure 10. Sound field when a secondary dipole is close to the primary source

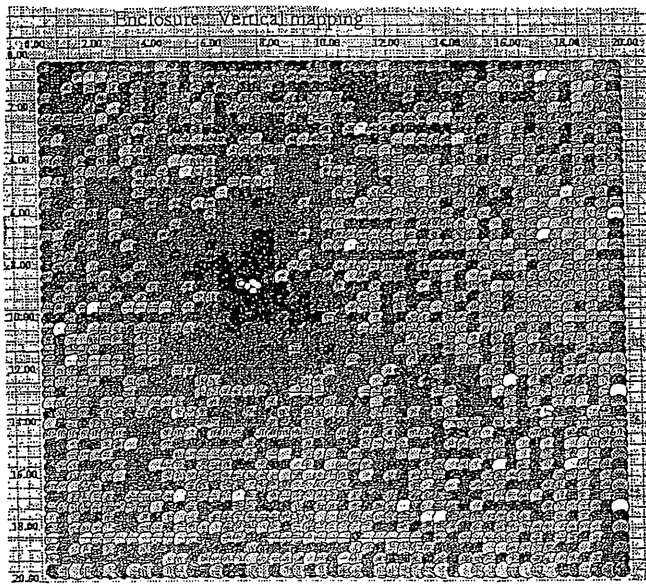

Figure 11. Sound field when a secondary quardrupole is close to the primary source

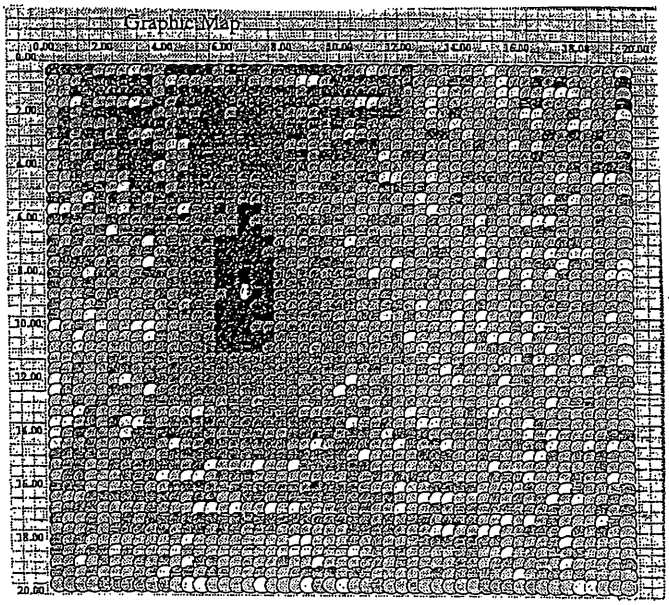

Figure 12. Sound field when two secondary monopoles of half the strength of the primary source each are close to the primary source

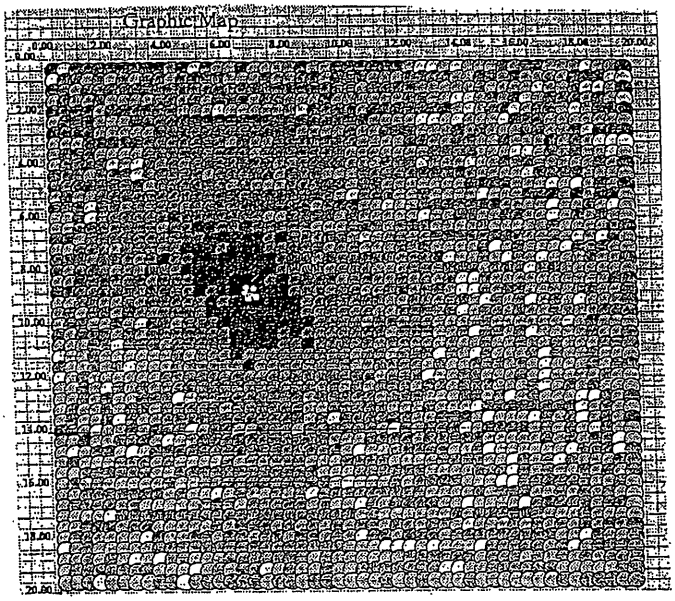

Figure 13. Sound field when five secondary monopoles of fifth the strength of the primary source each are close to the primary source

Theoretical and Computational Acoustics
D. Lee, Y-H Pao, M.H. Schultz, and Y-C Teng (Editors)

Model-Based Internal Wave Processing

J.V. Candy and D.H. Chambers
Lawrence Livermore National Laboratory

MODEL-BASED INTERNAL WAVE PROCESSING

J. V. Candy *D. H. Chambers*
Lawrence Livermore National Laboratory

A model-based approach is proposed to solve the oceanic internal wave signal processing problem that is based on state-space representations of the normal-mode vertical velocity and plane wave horizontal velocity propagation models. It is shown that these representations can be utilized to spatially propagate the modal (depth) vertical velocity functions given the basic parameters (wave numbers, Brunt-Vaisala frequency profile etc.) developed from the solution of the associated boundary value problem as well as the horizontal velocity components. Based on this framework, investigations are made of model-based solutions to the signal enhancement problem for internal waves.

I. INTRODUCTION

When operating in a stratified environment like the upper ocean with relatively sharp density gradients, then any excitation that disturbs the pycnocline (density profile) will generate *internal waves* that propagate away from this region (Apel,[1]). Internal waves are volume gravity waves having maximum vertical displacement typically at a plane where the density gradient are largest and are detectable far above and below this interface (Clay,[2]). They can be generated from tidal flow against islands, sea mounts and continental shelf edges or surface/internal wave interactions created displacements in the pyncocline. For instance, a ship traveling along the surface of a stratified ocean creates various visible wakes: the turbulent or centerline wake, the Kelvin wake and, of most interest in this work, the surface generated internal waves. Internal waves have been measured experimentally both in controlled environments as well as the open ocean (Garrett,[3]) and observed using synthetic aperture radar processing techniques from satellite imagery (Alpers,[4]; Thompson,[5]). From the scientific viewpoint, it is of high interest to understand the effect of internal waves on acoustic propagation in the ocean [2] as well as the ability to measure their effect directly using current sensor technology. Military applications are obvious, since a submerged body moving through the ocean environment disturbing the pyncocline generates internal wave signatures.

The inclusion of a propagation model in any oceanic signal processing scheme provides a means of introducing environmental information in a self-consistent manner. Recent work in ocean acoustics (Candy and Sullivan,[6]) has shown that a propagation model can be imbedded into a signal processing scheme to solve various enhancement, localization and detection problems. In this paper, we propose a model-based approach to the internal wave signal processing problem founded on a state-space representation of the normal mode and plane wave models of propagation. Specifically, using the normal mode model of the wave velocity field, the vertical velocity modal functions and the horizontal velocity can be estimated from noisy sensor array measurements in the following way. First, the propagation model is cast into state-space form. It is shown that this representation can be used to propagate the modal functions, given the basic parameters (wave numbers etc.) developed from the solution of the associated boundary value problem. There are basically two sets of equations in this representation: the state equation and the measurement

equation. The state equation describes the evolution in space of the vertical velocity modal and horizontal velocity functions, whereas the measurement equation relates the states to the actual array measurements. In the stochastic case, an approximate Gauss-Markov representation evolves. Once this framework is established, as will be shown in what follows, we investigate model-based solutions to the signal enhancement. We characterize a realizable, recursive processor as shown in Figure 1 (Candy,[7]; Jazwinski,[8]).

In the next section the state space representation of the internal wave propagation model is developed for both vertical and horizontal propagation. In the vertical, the so-called "forward propagator" is defined, while in the horizontal, plane wave propagators adequately characterize the propagation. Next the measurement equations are developed for both a vertical and then horizontal sensor array. The state-space model is then explicitly formulated for the case of all model parameters known where estimates of the velocity field and the modal functions are made and various noise models can be exercised in order to simulate different sources of modal and measurement noise. Next a dispersive internal wave model-based processor is designed which uses a horizontal array of sensors modeling the configuration employed in the Loch Linnhe experiments performed in Scotland during the summer of 1994. It is shown that the internal wave can be successfully estimated from noisy measurements. The final section summarizes the results.

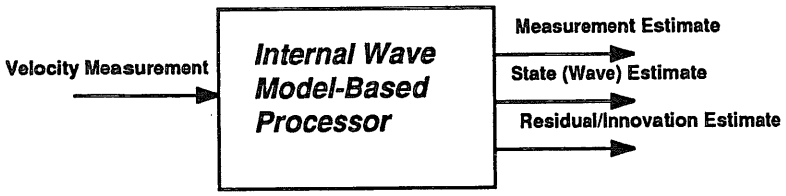

Figure 1. Basic Internal Wave Model-Based Processor.

II. INTERNAL WAVE STATE-SPACE PROPAGATION MODELS

In this section we investigate the feasibility of developing state-space propagation models from the corresponding internal wave dynamics. The development of the wave equation associated with internal wave propagation evolves from the small perturbation momentum equations under the assumptions of linearity, incompressibility, zero mean shear, a Boussinesq fluid, flat or slowly varying ocean bottom, and a horizontally homogeneous or slowly varying density field. Under these assumptions, the small perturbation component momentum equations governing the propagation of the *vector* velocity field defined are by $\chi(x,y,z,t) := [u(x,y,z,t)v(x,y,z,t)w(x,y,z,t)]'$ where u, v, w represent the respective *on-track velocity*, *cross-track velocity*, and *vertical velocity* components of the vector velocity field.

The solution to the homogeneous wave equation is accomplished by using the separation of variables approach (see Apel,[1]) with velocity function given by $w(x,y,z,t) = \mu(x)\nu(y)\phi(z)\tau(t)$.

where plane wave propagation in the respective horizontial dimensions, μ and ν are identical, ϕ is the vertical distribution and τ is the corresponding temporal function. Substituting, collecting terms, etc., it is possible to show that the function associated with each independent variable can be separated yielding a set of coupled ordinary differential equations with the corresponding separation constants shown as

$$\begin{aligned} \frac{d^2}{dx^2}\mu(x) + \kappa_x^2\mu(x) &= 0 \\ \frac{d^2}{dy^2}\nu(y) + \kappa_y^2\nu(y) &= 0 \\ \frac{d^2}{dz^2}\phi(z) + \kappa_h^2\left(\frac{N^2(z)}{\omega^2} - 1\right)\phi(z) &= 0 \\ \frac{d^2}{dt^2}\tau(t) + \omega^2\tau(t) &= 0 \end{aligned} \tag{1}$$

where κ_x and κ_y are the horizontal wave numbers with $\kappa_h^2 = \kappa_x^2 + \kappa_y^2$, and ω^2 the temporal frequency (a function of κ_h). These relations describe the dynamics of the vertical velocity component of an internal wave in a constant depth ocean. It is clear that the first two and last equations above admit harmonic solutions, that is, $\mu(x) = e^{i\kappa_x x}$ $\nu(y) = e^{i\kappa_y y}$ $\tau(t) = e^{-i\omega t}$ while the depth relation is an eigen-equation in z with

$$\frac{d^2}{dz^2}\phi_m(z) + \kappa_h^2\left(\frac{N^2(z)}{\omega_m^2} - 1\right)\phi_m(z) = 0, \qquad m = 1, \cdots, M \tag{2}$$

whose eigen-solutions $\{\phi_m(z)\}$ are the so-called *modal functions* associated with the vertical velocity component, κ_h is the *horizontal wavenumber*, $N(z)$ is the *Brunt-Vaisala frequency* profile (BVP) and ω_m is the corresponding *eigenvalue* associated wtih the m^{th}-modal function. State-space models will eventually be employed as "forward" propagators in model-based signal processing schemes (Candy,[7]). Note that this approach does *not* offer a new solution to the resulting boundary value problem, but, in fact, it requires that solution be available *a-priori* in order to propagate the normal-modes recursively in an initial value scheme.

Since Eq. 2 is a linear, space-varying coefficient (for each layer) differential equation, it can easily be placed in state-space form where the state-vector for each mode is defined as $\mathbf{x}_m := [\phi_m(z) \quad \frac{d}{dz}\phi_m(z)]'$. Examining mode propagation in more detail, we see that each mode is characterized by a set of ordinary differential equations which can be written as

$$\frac{d}{dz}\mathbf{x}_m(z) = A_m(z)\mathbf{x}_m(z) + B_m(z)\mathbf{u}_m(z) = \begin{bmatrix} 0 & 1 \\ -\kappa_h^2\left(\frac{N^2(z)}{\omega_m^2} - 1\right) & 0 \end{bmatrix}\mathbf{x}_m(z) + \begin{bmatrix} 0 \\ 1 \end{bmatrix}\mathbf{u}_m(z) \qquad (3)$$

where $\mathbf{u}(z) = \frac{ds(z)}{dz}$ is the source driving function (a scalar in our problem). With the parameters $[\{\kappa_h\}, N(z), \{\omega_m\}]$ known, we see that we have constructed a *forward propagator* for this problem driven by the source and initial condition vector, $\mathbf{x}_m(z_0)$ for each mode. From linear systems theory (see Chen,[9]), it is well-known that the general solution to this equation is governed by the state-transition matrix, $\Phi(z, z_0)$, where the state equation is solved by

$$\mathbf{x}_m(z) = \Phi_m(z, z_0)\mathbf{x}_m(z_0) + \int_{z_0}^{z} \Phi_m(z, \alpha)B_m(\alpha)\mathbf{u}_m(\alpha)d\alpha, \qquad m = 1, \ldots, M \qquad (4)$$

and the state transition matrix satisfies

$$\frac{d}{dz}\Phi_m(z, z_0) = A_m(z)\Phi_m(z, z_0), \qquad m = 1, \ldots, M \qquad (5)$$

with $\Phi_m(z_0, z_0) = I$.

If we include all of the M-modes in the model, then we obtain

$$\frac{d}{dz}\mathbf{x}_w(z) = \begin{bmatrix} A_1(z) & \cdots & O \\ \vdots & & \vdots \\ O & \cdots & A_M(z) \end{bmatrix}\mathbf{x}_w(z) + \begin{bmatrix} B_1(z) \\ \vdots \\ B_M(z) \end{bmatrix}\mathbf{u}(z) \qquad (6)$$

or simply

$$\frac{d}{dz}\mathbf{x}_w(z) = A(z)\mathbf{x}_w(z) + B(z)\mathbf{u}(z) \qquad (7)$$

The general solution to these modal state-space vertical velocity propagation equations are given by Eq. 10 over all the modes as

$$\mathbf{x}(z) = \Phi(z, z_0)\mathbf{x}(z_0) + \int_{z_0}^{z} \Phi(z, \alpha)B(\alpha)\mathbf{u}(\alpha)d\alpha \qquad (8)$$

and as before the state transition matrix satisfies

$$\frac{d}{dz}\Phi(z,z_0) = A(z)\Phi(z,z_0), \qquad \Phi(z_0,z_0) = I \tag{9}$$

with $\Phi(z,z_0) = diag[\Phi_1(z,z_0),\cdots,\Phi_M(z,z_0)]$.

The solutions in the other horizontal dimensions, x, y are also possible in state-space form, if desired, and take on the same form for each relation with the separation constants interchanged. For instance, the component $\nu(y)$ satisfies the following state equations with the state vector defined as $\mathbf{x}(y) := [\nu(y) \quad \frac{d}{dy}\nu(y)]'$

$$\frac{d}{dy}\mathbf{x}(y) = A_y\mathbf{x}(y) \tag{10}$$

where

$$A_y := \begin{bmatrix} 0 & 1 \\ -\kappa_y^2 & 0 \end{bmatrix} \tag{11}$$

which gives the plane wave solution of Eq. 7 above. We note that in this formulation the *strain rate*, which is an important quantity for radar images, appears as a component of the state vector. Thus, we see that using the state-space formalism enables us to characterize the propagation (forward) of the vertical internal wave velocity component which will prove useful for processing. Next we consider characterizing the corresponding measurement system.

Sensor technology enables us to measure components of internal wave cross-track velocity at depth z, $v(x,y,z,t)$ as well as on-track velocity $u(x,y,z,t)$. Let us investigate the deployment of a horizontal array of current meter sensors positioned to measure the cross-track velocity. Actual sensors sample the cross-track velocity in time at given spatial positions. To obtain the sensor output we must specify the functions $\mu(x)$, $\nu(y)$, and $\tau(t)$ as well as $\phi_v(z)$. The measurement at the n^{th} horizontal sensor at the location (x_n,y_n,z_ℓ) is given by

$$v(x_n,y_n,z_\ell,t) = \mu(x_n)\nu(y_n)\phi_v(z_\ell)\tau(t) = A\left(\frac{\kappa_y}{\kappa_h^2}\frac{d\phi(z_\ell)}{dz}e^{i(\kappa_x x_n+\kappa_y y_n-\omega(\kappa_h)t+\pi/2)}\right) \tag{12}$$

where A is a complex amplitude, and $\omega(\kappa_h)$ is the angular frequency which is a function of the wave

number magnitude given by, $\kappa_h = \sqrt{\kappa_x^2 + \kappa_y^2}$. The sensor measures the real part of the velocity field so we can write (using the magnitude phase form of A)

$$v(x_n, y_n, z_\ell, t) = -|A| \frac{\kappa_y}{\kappa_h^2} \frac{d\phi(z_\ell)}{dz} \sin(\kappa_x x_n + \kappa_y y_n - \omega(\kappa_h)t + \theta) \tag{13}$$

Since we have M-modal velocities, then (as before)

$$v(x_n, y_n, z_\ell, t) = \mathbf{C_y^T x}(z_\ell) \tag{14}$$

with $\mathbf{C_y^T} = \frac{\kappa_y}{\kappa_h^2}[0 \;\; \sigma_1(x,y,t) \;\; |\cdots| \;\; 0 \;\; \sigma_M(x,y,t)]$, and $\sigma_m(x_m, y_m, t) = |A_m| \sin(\kappa_x x_n + \kappa_y y_n - \omega_m(\kappa_h)t + \theta_m)$.

Incorporating *both* the vertical and horizontal state-space representations simultaneously leads to the set of coupled equations:

$$\begin{aligned} \tfrac{d}{dz}\mathbf{x}_w(z) &= A(z)\mathbf{x}_w(z) + B(z)\mathbf{u}(z) \\ \phi(z_\ell) &= \mathbf{C}_\phi^T \mathbf{x}_w(z_\ell) \end{aligned} \tag{15}$$

where $\mathbf{C}_\phi^T = \frac{\kappa_y}{\kappa_h^2} e^{i\pi/2}[0 \;\; 1 \;\; |\cdots| \;\; 0 \;\; 1]$

$$\begin{aligned} \tfrac{d}{dy}\mathbf{x}(y) &= A_y \mathbf{x}(y) \\ \nu(y_n) &= \mathbf{C}_\nu^T \mathbf{x}(y_n) \end{aligned} \tag{16}$$

with $\mathbf{C}_\nu^T = [1 \;\; 0 \;\; |\cdots| \;\; 1 \;\; 0]$ and the overall velocity measurment is

$$\begin{aligned} v(x, y_n, z_\ell, t) &= \nu^T(y_n)\mathbf{C}_v(x,t)\phi_v(z_\ell) \\ \mathbf{C}_v(x,t) &= diag[A_1\mu_1(x)\tau_1(t) \cdots A_M\mu_M(x)\tau_M(t)] \end{aligned} \tag{17}$$

which is the equivalent of a two-dimensional measurement taking into account both vertical and horizontal velocity measurements. So we see that the state-space representations enables alot of flexibility in modeling both the phenomenology (internal wave dynamics) as well as the accompanying measurement systems.

This constitutes a complete deterministic representation of the normal-mode and plane wave models in state-space form. However, since propagation in the ocean is effected by inhomogeneities in the water, slow variations in the BVP and motion of the surface, the model must be modified in order to include these effects. This can be done in a natural way by placing the model into a Gauss-Markov representation which includes the second order statistics of the measurement as well as the velocity noise. The measurement noise can represent the near-field velocity noise field, flow noise on the current meter and electronic noise. The modal noise can represent BVP errors, distant shipping noise, errors in the boundary conditions, sea state effects and ocean inhomogeneities. Besides the ability to lump the various noise terms into the model, the Gauss-Markov representation provides a framework in which the various statistics associated with the model such as the means and their associated covariances can be computed. This completes the state-space respresentations of internal wave dynamics. Next we investigate horizontal solutions using dispersive plane wave representations in the next section, develop the model-based processor, perform various simulations and apply the results to actual measurement data.

III. CROSS-TRACK VELOCITY ESTIMATION

In this section we use a model developed for the nondispersive case [12] and extend it to the dispersive by including more sophisticated dispersion models based on some empirical results [13] and approximating the appropriate temporal derivative. To extend these results (approximately) to the dispersive case, that is, the case where the temporal frequency is no longer constant (narrowband) but varies temporally, we return to the original development of the plane wave processor of the previous section. Recall that the states were defined as, $\mathbf{x}(t) := [v(t)\frac{d}{dt}v(t)]^T$ and now from Eq. 45 with both frequency and wave number temporal functions, we have

$$v(y,t) = \cos(\kappa_y(t)y - \omega(t)t) = \cos\kappa_y(t)y\ \cos\omega(t)t + \sin\kappa_y(t)y\ \sin\omega(t)t \tag{18}$$

From our definition of the temporal state vector, we have that $\tau(t) := \cos\omega(t)t$ and approximate its corresponding derivative using

$$\frac{d}{dt}\tau(t) = -\omega(t)\left[1 + \frac{\dot{\omega}(t)}{\omega(t)}t\right]\sin\omega(t)t \approx -\omega(t)\sin\omega(t)t \tag{19}$$

Defining the notation for the dispersive case, we have for the ℓ^{th}-sensor

$$\alpha_\ell(t) := \cos\kappa_y(t)y_\ell, \qquad \beta_\ell(t) := \frac{\sin\kappa_y(t)y_\ell}{\omega(t)} \tag{20}$$

therefore, the measurement becomes

$$v(y_\ell, t) = \alpha_\ell(t)\cos\omega(t)t - \beta_\ell(t)\sin\omega(t)t = \alpha_\ell(t)\tau_1(t) - \beta_\ell(t)\omega(t)\tau_2(t) \tag{21}$$

Next we must develop the relations for the dispersive case. For a plane wave propagating in the y-direction, the value of wave number at time t is a function of *group speed* $c_g(\kappa_y)$, that is,

$$y_\ell = c_g\left(\kappa_y(t)\right) t \tag{22}$$

with corresponding temporal frequency $\omega(\kappa_y(t), t)$. Using the Barber approximation [13] for internal wave dispersion and group speed, we have

$$\omega(\kappa_y(t), t) = \frac{\kappa_y(t) C_o}{1 + \kappa_y(t) C_o / N_o} \tag{23}$$

and

$$c_g(\kappa_y(t)) = \frac{C_o}{(1 + \kappa_y(t) C_o / N_o)^2} \tag{24}$$

Substituting Eq. 24 for c_g in Eq. 22 and solving for the wave number at the ℓ^{th}-sensor, we obtain

$$\kappa_y(t) = \frac{N_o}{C_o}\left(\sqrt{\frac{C_o t}{y_\ell}} - 1\right) \tag{25}$$

Substituting this result into Eq. 23, the corresponding temporal frequency is given by

$$\omega_\ell(t) = N_o\left(1 - \sqrt{\frac{y_\ell}{C_o t}}\right) \qquad t > \frac{y_\ell}{C_o} \tag{26}$$

Further assuming a bandlimited pulse with minimum frequency ω_o and observation time at the ℓ^{th}-sensor given by

$$t_{o\ell} = \frac{y_\ell}{C_o(1 - \omega_o / N_o)^2} \tag{27}$$

and defining the time index as $t = t_{o\ell} + t_k$, $t_k > 0$, then we can obtain an expression for the temporal frequency as

$$\omega_\ell(t_k) = N_o \left(1 - \frac{1 - \omega_o/N_o}{\sqrt{1 + \frac{C_o t_k}{y_\ell} (1 - \omega_o/N_o)^2}} \right) \qquad t_k > 0 \tag{28}$$

It should be denoted that this dispersive model is based on the fact that the onset has been detected, that is, the appropriate time delays estimated. In our case we use Eq. 27 to calculate the appropriate delays once an onset is established at the specified sensor. When we show the measured experimental data, it should be noted that we selected this onset time and then applied the processor. A more sophisticated approach would be to find the "optimal" onset based on these models, but this is left for future work. Now if we return to the central difference form for the equations, we obtain the approximate *spatially-constrained, dispersive* state-space representation

$$\mathbf{x}(t_{k+1}) := \begin{bmatrix} 1 - \omega(t_k)^2 \Delta t^2 & \Delta t & | & & \\ -\omega(t_k)^2 \Delta t & 1 & | & O & \\ - & - & & - & - \\ & & \ddots & & \\ - & - & & - & - \\ & O & | & 1 - \omega(t_k)^2 \Delta t^2 & \Delta t \\ & & | & \omega(t_k)^2 \Delta t & 1 \end{bmatrix} \mathbf{x}(t_k), \tag{29}$$

and with corresponding discrete cross-track velocity array measurements (in this coordinate system)

$$\mathbf{v}(t_k) := \begin{bmatrix} \alpha_1(t_k) & -\beta_1(t_k) & | & O & \\ - & - & & - & - \\ & & \ddots & & \\ - & - & & - & - \\ & O & | & \alpha_L(t_k) & -\beta_L(t_k) \end{bmatrix} \mathbf{x}(t_k) \tag{30}$$

In this coordinate system the initial condition vector is given by

$$\mathbf{x}(t_o) = \begin{bmatrix} 1 \\ 0 \\ - - - \\ \vdots \\ - - - \\ \cos(\kappa_y(L-1)\Delta) + \omega(t_k)\Delta t \sin(\kappa_y(L-1)\Delta) \\ \omega(t_k) \sin(\kappa_y(L-1)\Delta) \end{bmatrix}, \tag{31}$$

With this approximate dynamic dispersive model, we developed a Gauss-Markov simulation with the corresponding frequency and wave numbers varying temporally according to the dispersion relation. This presents no particular problem in the Gauss-Markov formulation, since it can support nonlinear dynamics as well as nonstationary statistics. We performed the simulation with the same basic set of parameters and the results for a $-13dB$ SNR were quite successful indicating an optimal design.

Next we consider the application of the dispersive model-based processor to an internal wave field experiment performed in Loch Linnhe, Scotland in September of 1994 (Mantrom,14]; Robey,[15]). The general objective of this experiment is to examine the relationship between modulations observed in radar images and ship generated, internal waves by fusing the data with that measured by an array of current meter sensors. Loch Linnhe is a narrow, salt water estuary located on the west coast of Scotland which possesses favorable subsurface environmental conditions (stratification) which are conducive for the generation and propagation of internal waves. The internal waves are generated by surface ships with concurrent oceanographic measurements (temperature, salinity, BV frequency, meterology, etc.) performed by other vessels in the Loch. Internal waves are typically imaged by airborne radar systems employing synthetic aperture radar techniques; however, this experiment concentrated on real aperture radar images of the waves from low-grazing angle marine radars positioned on the surrounding hillsides and an array of current meter sensors which provide measurements of hydrodynamic currents associated with the internal waves. The Lawrence Livermore National Laboratory (LLNL) current meter array (CMA) measurement platform consists of ten (10) standard S4 current meters uniformly spaced at $3.75m$, longitudinally, creating a $34m$ aperture, positioned at a depth of $2m$ and sampled at a $10sec$ rate. The CMA is positioned to measure both cross-track and on-track velocities. A typical measurement is shown in Figure 3a, where we see the output of each sensor channel typifying the phase front of an internal wave and subsequent ambient noise.

We processed the Loch Linnhe expermental data using the dispersive rather than plane wave processor and the results are shown in Figure 2. Here we see the differences in using the dispersive over the nondispersive approach. First, the processing doesn't really begin until the "onset" has begun and then the MBP utilizes the dispersive model, until that time a simple random walk model is employed (constant + gaussian noise). Next we note that each internal wave component temporal signal is clearly visible especially those which meet the onset criterion established by the dispersion relation. Those non-propagating wavefronts are attenuated quite heavily. We see the enhanced internal wave propagating across the array based on the onset and all other events attenuated significantly. We note the overall selectivity of the MBP to events that "match" both its dispersive signal model as well as onset. This completes the development of the dispersive MBP for internal wave enhancement and its application to experimental data, we summarize our results and place them in perspective.

IV. DISCUSSION

We have developed the model-based approach to processing internal waves. It was shown

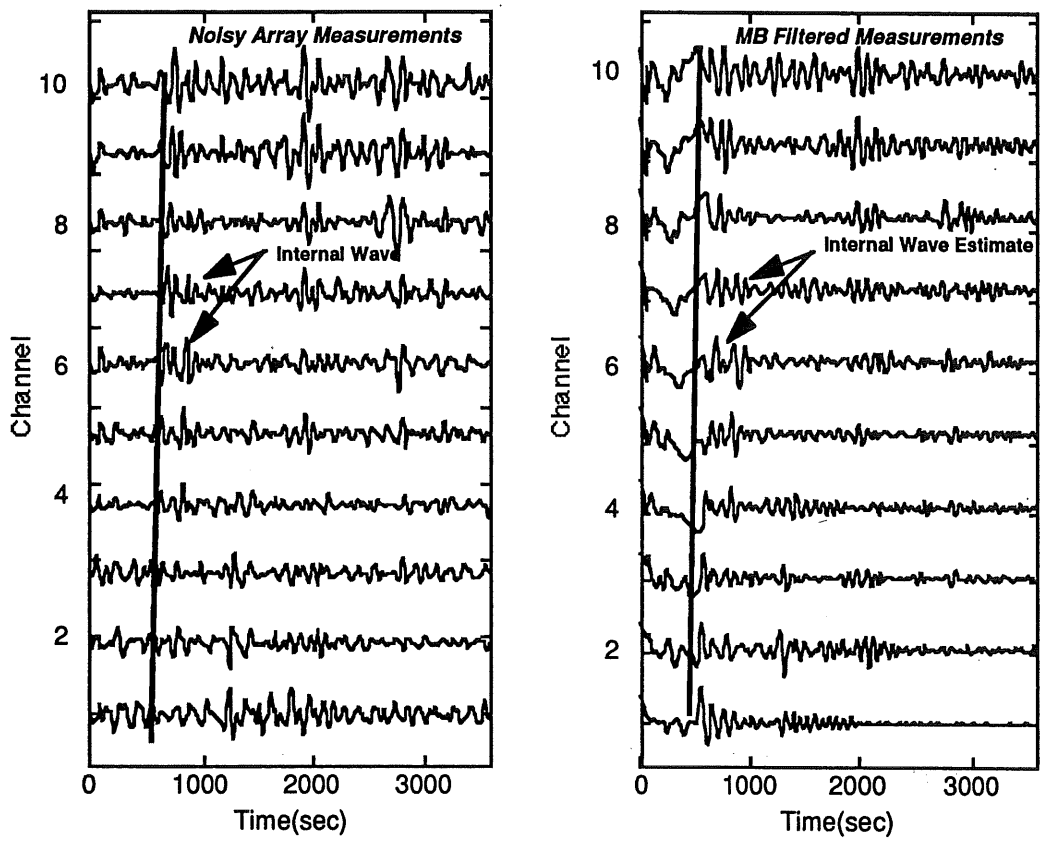

Figure 2. Dispersive Wave MBP Design for Loch Linnhe Experimental Array (10-elements): (a) Preprocessed Sensor Signals (s7r1). (b) Enhanced Sensor Estimates.

how to develop the underlying state-space representations of the internal wave propagation model. In the vertical, a normal-mode propagation model resulted, while in the corresponding horizontal plane wave propagation models were developed. Since our primary motivation was to process measurements from a horizontal array of current meter sensors, we developed the horizontal (plane wave) processors for both the nondispersive and dispersive cases. After using the model to develop Gauss-Markov stochastic simulations, the model-based processors were designed using the extended Kalman filter (EKF) algorithm [7] for signal enhancement. After designing the MBP, the minimum variance estimates were shown capable of extracting the desired wavefronts from simulated data quite effectively.

We then applied the various MBP to sets of data gathered from experiments performed in Loch Linnhe, Scotland during the summer of 1994 [14,15] and the results are quite promising. It was shown that the nondispersive plane wave MBP was capable of selecting all wave fronts that matched the correct temporal frequency and prescribed onset arrival times while attenuating all others. The dispersive MBP design approximated the true dispersive solution for slow changes in temporal frequency and appears to be a more effective approach, since it depends heavily on the pre-specified wavefront onset arrivals at the array and therefore is more discriminating then the nondispersive design.

References

[1] J. R. Apel, *Principles of Ocean Physics*, New York:Academic Press, 1987.

[2] C. S. Clay, and H. Medwin, *Acoustical Oceanography.* New York:Wiley, 1977.

[3] C. Garrett and W. Munk, "Internal waves in the ocean." *Ann. Rev. Fluid Mech.*, **11**, 339-369, 1979.

[4] W. Alpers, "Theory of radar imaging of internal waves." *Nature*, **314**, 245-247, 1985.

[5] D. R. Thompson and R. F. Gasparovic, "Intensity modulation in SAR images of internal waves". *Nature*, **320**, 345-348, 1986.

[6] J. V. Candy and E. J. Sullivan. "Ocean acoustic signal processing: a model-based approach." *J. Acoust. Soc. Am.*, **92**, (12), 3185-3201, 1992.

[7] J. V. Candy, *Signal Processing: The Model-Based Approach.* New York:McGraw-Hill, 1986.

[8] A. Jazwinski, *Stochastic Processes and Filtering Theory.* New York:Academic Press, 1970.

[9] O. M. Phillips, *The Dynamics of the Upper Ocean*, Cambridge:Cambridge Univ. Press, 1977.

[10] C. T. Chen, *Introduction to Linear System Theory.* New York:Holt, Rinehart and Winston, 1970.

[11] G. J. Bierman, *Factorization Methods of Discrete Sequential Estimation.* New York:Academic Press, 1977.

[12] E. J. Sullivan and J. V. Candy. "Passive synthetic aperture processing as a Kalman filtering problem." *J. Acoust. Soc. Am.*, **95**, (5), Part 2, 2953, 1994.

[13] J. V. Candy and P. M. Candy, "SSPACK_PC: A model-based signal processing package on personal computers," *DSP Applic.*, **2**,(3), 33-42, 1993.

[14] B. C. Barber, "On the dispersion relation for trapped internal waves," *J. Fluid Mechanics.*, **252**, 31-49, 1993.

[15] D. D. Mantrom, "Loch Linnhe '94: Test Operations Description and On-Site Analysis US Activities," *LLNL Report.*,UCRL-ID-119197, 1994.

[16] H. F. Robey and D. L. Ravizza, "Loch Linnhe Experiment 1994: Background Stratification and Shear Measurements Part 1: Profile Summary and Dispersion Relations", *LLNL Report.*,UCRL-ID-119352, 1994.

Acknowledgements: We would like to acknowledge the motivation and support of Dr. R. Twogood, Program Leader LLNL Advanced Applications Program and Mr. James Brase, Project Leader for Radar Ocean Imaging. We also gratfully acknowledge our colleagues for the many clarifications and technical discussions: Dr. D. Holliday, Mr. H. Jones, Mr. D. Mantrom and Dr. H. Robey. This work was performed under the auspices of the Department of Energy by the Lawrence Livermore National Laboratory under contract W-7405-Eng-48 and supported by the Office of the Secretary of Defense.